Proceedings of ASME Turbo Expo 2011
GT2011
June 6-10, 2011, Vancouver, British Columbia, Canada

GT2011-46322

DIRECT NUMERICAL SIMULATIONS OF WAKE-PERTURBED SEPARATED BOUNDARY LAYERS

Ayse G. Gungor *, **Mark P. Simens, and Javier Jiménez**

School of Aeronautics
Universidad Politécnica de Madrid
Madrid, 28040
Spain
Email: gungor@torroja.dmt.upm.es

ABSTRACT

A wake-perturbed flat plate boundary layer with a streamwise pressure distribution similar to those encountered on the suction side of typical low-pressure turbine blades is investigated by direct numerical simulation. The laminar boundary layer separates due to a strong adverse pressure gradient induced by suction along the upper simulation boundary, transitions and reattaches while still subject to the adverse pressure gradient. Various simulations are performed with different wake passing frequencies, corresponding to the Strouhal number $0.0043 < f\theta_b/\Delta U < 0.0496$ *and wake profiles. The wake profile is changed by varying its maximum velocity defect and its symmetry. Results indicate that the separation and reattachment points, as well as the subsequent boundary layer development, are mainly affected by the frequency, but that the wake shape and intensity have little effect. Moreover, the effect of the different frequencies can be predicted from a single experiment in which the separation bubble is allowed to reform after having been reduced by wake perturbations. The stability characteristics of the mean flows resulting from the forcing at different frequencies are evaluated in terms of local linear stability analysis based on the Orr-Sommerfeld equation.*

NOMENCLATURE

C_f	Skin friction coefficient $\tau_w/\frac{1}{2}\rho U_{ref}^2$
C_p	Pressure coefficient $(P-P_{ref})/(0.5\rho U_{ref}^2)$
H	Shape factor δ^*/θ
L_b	Length of the separated region $[m]$
L_{b_0}	Length of the unforced separated region $[m]$
L_x, L_y, L_z	Domain length in x,y,and z
N_x, N_y, N_z	Number of grid points in x,y,and z
Re	Reynolds number $U_{ref}\theta/\nu$
St	Strouhal number fL_x/U_{ref}
St_{θ_b}	Strouhal number $f\theta_b/\Delta U$
U_{ref}	Reference velocity at the inflow $[ms^{-1}]$
f	Wake passing frequency $[Hz]$
δ^*	Displacement thickness $[m]$
θ_0	Momentum thickness at inlet $[m]$
θ_e	Momentum thickness at exit $[m]$
θ_s	Momentum thickness at separation $[m]$
λ	Wavelength $[m]$
Λ_s	Pressure gradient parameter at separation $\frac{\theta_s^2}{\nu}\frac{dU_e}{dx}\|_s$
ν	Kinematic viscosity $[m^2s^{-1}]$
$\mathscr{T}$	Wake passing period $1/f$

INTRODUCTION

Separated boundary layers subjected to strong adverse pressure gradients (APG) and forced by incoming wakes are of great

*Address all correspondence to this author.

practical interest. Understanding the influence of the wakes on the onset of separation and reattachment and investigating the dependence of the separated region on the presence of large scale forcing have considerable practical significance, since they are related to the efficiency of many aerodynamic devices, like turbine blades. There have been several simulations [1,2] and experimental studies [3] on the subject, but more fundamental research is necessary to understand how the wakes influence the APG flows, and in particular the influence of wakes on separated flow.

Many recent studies focus on identification of the dominant transition mechanism in the unstable separated shear layer. In a two-dimensional numerical study by [4], the unsteadiness of the laminar separation bubble was found to form from a shedding of vortices from the bubble. This was attributed to the inviscid instability of the separated shear layer. A detailed experimental study of a two-dimensional separation bubble was carried out by [5]. The stability characteristics were investigated by introducing wave packets into the boundary layer. It was concluded that the primary instability is an inviscid inflectional Kelvin-Helmholtz instability. A comprehensive review of the stability characteristics of a separation bubble is presented in [6]. Based on their linear stability calculations for analytical velocity profiles representing the profiles around the bubble, they showed that the instability of the separated shear layer is similar to the instability of the free-shear layer. Direct numerical simulation (DNS) of a short bubble is studied in [7], where it is concluded that the separated shear layer undergoes transition via oblique modes and lambda-vortex-induced breakdown.

The general difficulty in the study of this flow is the existence of a wide range of parameters that might play a role, such as the upstream turbulence, the pressure gradient and its functional form, and the parameters related to the wakes. For example, little is known about what the important wake parameters are: whether their mean profiles, their small-scale velocities, or both? The periodic unsteady nature of incoming wakes substantially influences the boundary layer development, including the onset and extent of the laminar separation and its turbulent attachment. There are several numerical studies [2] that investigate the effect of small-scale fluctuation inside the wake on the separation and reattachment locations. It was observed that the transition to turbulence, hence the reattachment location, depend on the presence of small-scale fluctuations inside the wake, whereas it does not affect the initial inviscid instability mechanism, which is triggered due to the mean wake deficit. It is important to understand the mechanism by which the upstream wakes in low-pressure turbines delay separation. The main unanswered question is not so much how long it takes for the boundary layer to re-adhere when the wakes come, but how long it takes to re-separate again after the wake has passed. The purpose of this study is to contribute to the understanding of the physics of the flow in a turbine passage, and to provide reference data for the development of advanced design methods and turbulence models.

This paper is organized as follows: after describing the numerical setup we discuss in detail the effect of wake passing frequency on the separated flow. Results of various performed simulations, in which the wake passing frequency is varied, are presented in two subsections: first the development of some flow parameters in each phase of the forcing are discussed, and later the important statistical quantities are presented. In the following part the influence of the wake profile on the flow is discussed. Finally, we describe a single numerical experiment that can be used to predict the effect of the different wake passing frequencies, consisting in switching off the wake forcing, and allowing the separation bubble to regenerate to the unforced situation. Furthermore a linear stability analysis (LSA) is performed and its results are related to the DNS results. The paper ends with conclusions.

NUMERICAL EXPERIMENTS

The model that we are using in this study is a flat plate with a streamwise pressure distribution similar to those encountered on the suction side of turbine blades. The unforced base flow was chosen to match the experiment in [8], in which a flat plate was set in a convergent-divergent wind tunnel designed to reproduce the same pressure gradient as on the suction side of a T106C ultra-high-lift LP turbine blade. Our simulations match the APG part of that experiment, including the Reynolds number and the inflow conditions, which were found to be very close to a laminar Hiemenz profile. Curvature effects are not important in this part of the blade, which is typically flat [3]. For example, [8] also includes experiments on a real T106C cascade, and they mention that the length of the separation bubble agrees in both cases, although the separation itself is slightly delayed on the plate.

The Reynolds number at the inlet of the simulation, based on the inflow momentum thickness $\theta_0 = 0.268$mm, and on the free-stream velocity $U_{ref} = 6.3$m/s, is $Re_{\theta_0} \approx 110$, which is low enough to be in the realm of expensive DNS.

The code uses a fractional step method on a staggered grid, with third-order Runge-Kutta time-integration, fourth order compact spatial discretization for the convective and viscous terms, and second order discretization for the pressure in the directions perpendicular to the span, which is spectral. The result is second-order-accurate for the velocities, but with an almost-spectral resolution of the derivatives. The unforced simulation is described in [9,10], including resolution studies, a full discussion of the numerical scheme, and comparison with the available experimental data.

The simulation domain, $(L_x \times L_y \times L_z)/\theta_0 = 1640 \times 468 \times 123$, is discretized in $N_x \times N_y \times N_z = 1539 \times 301 \times 768$ collocation points, which was shown in [10] to result in grid cells of the order of the Kolmogorov length scale. It is important to note that scaling the grid in wall units is not very useful in separated flows, for which $u_\tau \approx 0$ at reattachment and separation. However, downstream of reattachment for the current simulations, $\Delta y^+ \approx 0.4$ at the wall, and $\Delta y^+ \approx 2$ further into the boundary layer, while $\Delta x^+ \approx \Delta z^+ \approx 2$. A variable time step was used, determined by a constant $\mathrm{CFL} = 0.6$ condition.

An almost constant suction velocity was imposed at the upper boundary to match the linear APG that makes the flow separate at the same streamwise position as in the experiment [8]. No-slip boundary conditions are applied on the wall and the spanwise direction is treated as periodic. At the outflow plane a convective boundary condition is used, with minor adjustment to the exit velocity to ensure global mass conservation.

For the forced cases, artificial wakes designed to mimic the mean wake deficit created by a linear row of cylinders [11] moving in the vertical direction are superimposed on the laminar Hiemenz profile. The fluctuations within the wakes are neglected. Steady three-dimensional perturbations are also explicitly added at the inflow for transition to occur, since otherwise spectral codes along the span, like the one used here, would remain strictly two-dimensional [9]. The Strouhal number based on the wake passing frequency, the momentum thickness of the unperturbed shear layer that forms between the separation bubble and the free-stream, and the velocity difference at the maximum reverse flow, St_{θ_b}, varies between 0 to 0.0496. The non-dimensional frequency can also be based on the length of the plate and the reference velocity at the inlet, St, which is used in the experimental study [8]. For the forcing frequencies considered here, St varies between 0 to 2.9. The two low-St cases, 0.25 and 0.78 ($St_{\theta_b} = 0.0043$ and 0.0133), that are investigated in this study, to be presented in the next section, are approximately of the order of the operating conditions of a low-pressure-turbine.

STROUHAL NUMBER EFFECT

The size of the separated region is a complex function of Reynolds number and inflow perturbations. In order to reduce the number of parameters involved in the problem, the inflow Reynolds number is fixed for all cases but the passing frequency and the shape of the forcing are varied. All the experiments presented in this section are done by varying the frequency of the forcing while keeping the shape of the inflow wakes constant. The incoming wakes are modeled to account for the wakes generated by a linear row of cylinders with a diameter $d = 31\theta_0$ moving at a spatial distance $x_w = -1738\theta_0$ to the inflow with a velocity $U_w = 0.83U_{ref}$. The maximum wake deficit is $0.13U_{ref}$ and the mean wake half-width is $130\theta_0$. The parameters of the numerical experiments as a result of varying the forcing frequency are given in table 1.

TABLE 1. Parameters of the Strouhal number experiments and characteristics of the separated regions.

Case	St_{θ_b}	St	Re_{θ_e}	Re_{θ_s}	Λ_s	L_b/L_{b_0}
$\mathscr{W}0$	0	0	1600	161	-0.083	1.0
$\mathscr{W}1$	0.0043	0.25	1120	167	-0.104	0.8777
$\mathscr{W}2$	0.0133	0.78	1056	165	-0.113	0.4378
$\mathscr{W}3$	0.0176	1.03	1030	167	-0.117	0.4148
$\mathscr{W}4$	0.0265	1.55	980	167	-0.118	0.3810
$\mathscr{W}5$	0.0496	2.90	950	168	-0.171	0.3645

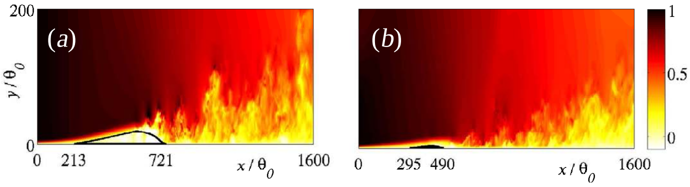

FIGURE 1. Instantaneous streamwise velocity: (a) $\mathscr{W}0$; (b) $\mathscr{W}4$. The black solid line indicates the separation bubble.

The unsteadiness in the perturbed flow can be split into mean, stochastic, and periodic component, the later associated with the forcing. Thus, the instantaneous velocity U_i can be written as $U_i = \overline{U_i} + \tilde{u}_i + u_i$ where $\overline{U_i}$ is the time-averaged velocity, $\tilde{u}_i$ is the periodic velocity fluctuation, and u_i is the remaining velocity fluctuations. The phase-averaged velocity $\langle U_i \rangle$ is the sum of the time-averaged velocity and the periodic velocity fluctuations, $\langle U_i \rangle = \overline{U_i} + \tilde{u}_i$. For all cases, the velocity field is allowed to evolve for about 10 wake passing periods, and statistics are collected for another 10 periods. The computational time is $43K$ CPU hours for one period of the $\mathscr{W}1$ case and $3K$ CPU hours for one period of the $\mathscr{W}5$ case. Statistics are formed by averaging in the spanwise direction as well as time. Phase averaging was performed by dividing each passing period into 200, 100, and 20 equal subdivisions for cases $\mathscr{W}1, \mathscr{W}2$, and $\mathscr{W}3 - \mathscr{W}5$, respectively.

When no wakes are present, the incoming flow is laminar, separates due to the adverse pressure gradient, transitions within the separated region, reattaches as a consequence of transition, and develops into an attached turbulent adverse-pressure-gradient boundary layer (see Fig. 1a). The periodically impinging wakes alter the boundary layer development, and the location of separation, transition, and reattachment (see Fig. 1b).

The conditions at the separation points lie within the range of values observed in previous studies. The Reynolds number based on the momentum thickness at the separation points Re_{θ_s} is about 167 and it is insensitive to the forcing frequency of the incoming wakes. This value is consistent with the ones obtained by [12], where Re_{θ_s} ranged from 136 to 432. At the separation point, the pressure gradient parameter [13], presented in table 1,

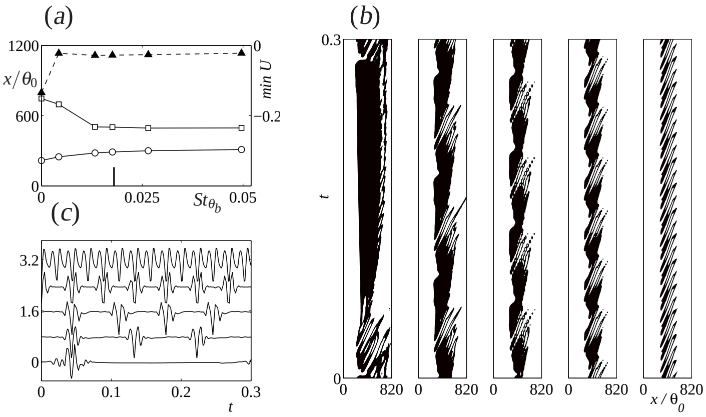

FIGURE 2. (a) Separation (○) and reattachment (□) points (left y-axis) and the minimum velocity (▲, right y-axis) as a function of St_{θ_b}. The vertical thick line indicates the Kelvin-Helmholtz frequency, $St_{\theta_b} = 0.018$. (b) The space-time development of the negative streamwise velocity at $y/\theta_0 = 0.17$ for cases $\mathscr{W}1 - \mathscr{W}5$ left to right, respectively. (c) The time history of the streamwise velocity at $y/\theta_0 = 0.17$ as a function of time at $x/\theta_0 = 426$, located inside the separated region, for cases $\mathscr{W}1 - \mathscr{W}5$ bottom to top, respectively. Data shifted vertically for visual clarity.

lies in the range $-0.171 < \Lambda_s < -0.083$. The unperturbed case compares quite well with the value of $\Lambda_s = -0.082$ suggested in [13]. Moreover, for all cases, the value of the pressure gradient parameter at the separation point is consistent with prior studies, ref. [14] found $-0.171 < \Lambda_s < -0.068$ for the onset of separation.

The Strouhal number based on momentum thickness at the maximum reverse flow St_{θ_b} (see table 1) shows that the frequencies for cases $\mathscr{W}2 - \mathscr{W}4$ are close to the frequencies of the most unstable Kelvin-Helmholtz frequencies [15, 16]. Figure 2a depicts the variation of the bubble length as a function of the Strouhal number. The bubble length drops significantly for frequencies around the Kelvin-Helmholtz frequency. As the frequency increases further, the size of the separated region still decreases but only slightly. For the low frequency case ($\mathscr{W}1$), there is enough time for the separated region to re-generate itself before the next wake arrives, hence the average size of the bubble did not change dramatically. However, even with this low-frequency forcing the separation and reattachment locations are affected. The dramatic effect of the forcing frequency can be clearly seen between cases $\mathscr{W}1$ and $\mathscr{W}2 - \mathscr{W}5$. The forcing frequency tripled from case $\mathscr{W}1$ to $\mathscr{W}2$ and the bubble size reduced almost 50%. It is interesting to note that for cases with St_{θ_b} numbers higher than 0.0133 the bubble size varies significantly in time, but due to the high wake passing frequency the longest instantaneous separated region is shorter than the one in the unperturbed case. Therefore the time-averaged length for these cases is shorter than the one in the unperturbed case or the ones in low Strouhal number cases.

The space-time evolution of the separated region is shown in Fig. 2b-c. All numerical experiments have a separated region whose size changes periodically due to the influence of incoming wakes. As the wake impacts the separated region, the separation bubble becomes unstable causing an increase in the level of mixing, which significantly reduces the separated region in size. Due to the enhanced mixing across the separated shear layer, the shear stress increases, effectively shortening but never completely eliminating the separation. After the wake passes, the separated region again increases in size before it is impacted by the next wake. All experiments show vortices originating at the top of the separated region. The space-time development of the negative U-velocity, depicted in Fig. 2b shows the paths followed by the strongest vortices, since the flow below them is locally separated. The wake impact modifies the separation bubble and induces roll-up vortices. The signature of the roll-up vortex does not appear immediately downstream of the separation onset location, which suggests that the vortex can only form when the separated shear layer is at a certain distance from the surface. These roll-up vortices convect downstream at about half of the local freestream velocity. For the wake-passing periods considered here, the data show that there are always three roll-up vortices following each other, which has been observed in experimental studies as well [17]. The reason for these three vortices is unknown, and needs to be examined in detail, since their formation and decay eventually turn into profile loss. A criterion based on the level of reverse flow in a separated shear layer is often used to assess whether an absolute instability is present in a separated region. A threshold of approximately 20% of the local freestream is identified by [7] above which absolute instability exists. In all the forced cases studied here the reverse-flow levels (see Fig. 2a) are much lower than this threshold, indicating that, if instability exists, it is convective rather than absolute. This will be investigated in detail later in the linear stability section.

Phase-Averaged Flow Properties

The sequence of phase-averaged spanwise vorticity contours along with spanwise velocity fluctuations for case $\mathscr{W}4$ shown in Fig. 3, provides a clear view of what happens around the separated region. For the wake passing period considered in this case, there are two wakes in the numerical domain. They are separated by a distance of $x/\theta_0 = 920$. Between these two wakes, there is not enough time for the bubble to regenerate itself. As the wake convects to the separated region, it interacts with the inflectional boundary layer, and triggers the Kelvin-Helmholtz instability that later leads to the development of roll-up vortices in the shear layer and to a breakdown of the laminar shear layer. The spanwise velocity fluctuation marks regions where there is significant three-dimensionality. As it can be deduced from Fig. 3, three-dimensional perturbations are amplified in the region of developing vortices. This development of three-dimensionality

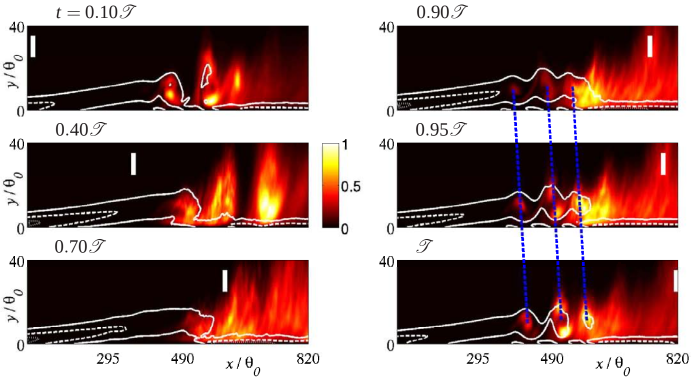

FIGURE 3. The phase-averaged spanwise velocity fluctuations (shaded contours ranging $0 < w_{rms}/w_{rms}|_{max} < 1$) and spanwise vorticity contours ($\omega_z/\omega_z|_{max}$ —, 0.1; – –, 0.3; ····, 0.5) over one forcing period The vertical thick solid line marks the location of the wake center. Dashed lines trace the development of roll-up vortices. The x axes labels 295 and 490 mark separation and reattachment points of the time-averaged bubble for case $\mathscr{W}4$.

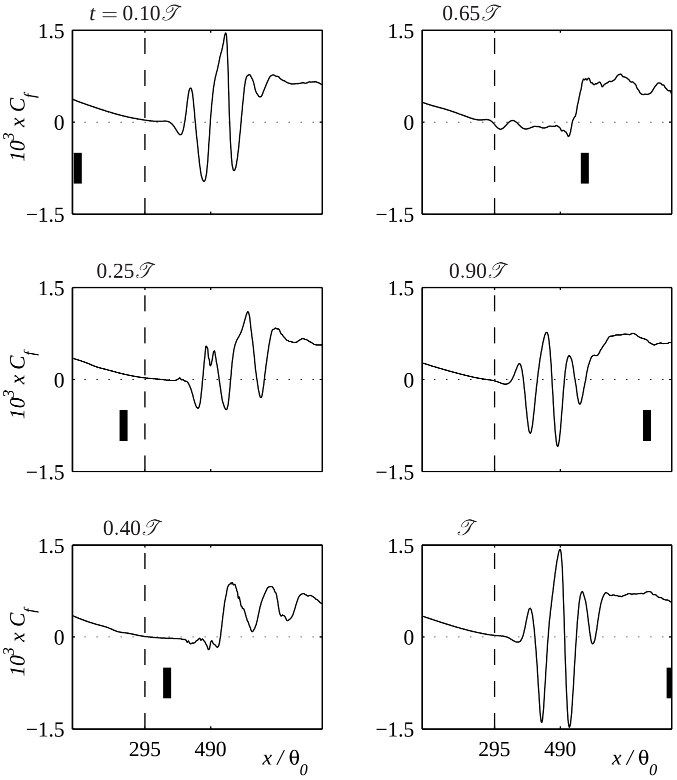

FIGURE 4. The phase-averaged skin-friction coefficient over one forcing period for case $\mathscr{W}4$. The vertical thick solid line marks the location of the wake center. The x axes labels 295 and 490 mark separation and reattachment points of the time-averaged bubble.

is the first stage in the transition process that eventually leads to the turbulence. When the wake moves farther into the turbulent region, the rolls of recirculating flow convect downstream where they are destroyed in the turbulent region. The phase-averaged skin friction coefficient, Fig. 4, shows the footprint of the vortices on the wall. The existence of distinct peaks and troughs within the separated region is recognized, and these coincide with large-scale positive and negative perturbations of the streamwise velocity in the near-wall associated with the vortices. The amplitudes of the skin friction fluctuations slowly decline as they are convected downstream.

As noted earlier, the point of separation moved downstream in the case of forcing due to the mean flow deformation. In order to clarify this we have looked at the phase-averaged momentum budget for case $\mathscr{W}4$. The streamwise momentum budget is given in Fig. 5 over a specific part ($t = 0.1\mathscr{T} - 0.65\mathscr{T}$) of one forcing period at $x/\theta_0 = 295$, which is the point of separation of the time-averaged flow for case $\mathscr{W}4$. The flow is not in equilibrium in all cases. Figure 5 shows that all the terms in the streamwise momentum equation, except the Reynolds stress with respect to the phase average, are important at this location. The Reynolds stress term starts to develop in the shear layer between the separation bubble and the free-stream. In all cases the viscous term is important both in the near-wall region, where it is in equilibrium with the pressure gradient, and in the separated shear layer. It can be seen that the advective term plays an important role in the streamwise momentum equation. The clearest effect of the wake is seen at $t = 0.2\mathscr{T}$. At this time the effect of the approaching wake front is clear at this location. The advective term in the outer region is positive. This indicates that the wake front accelerates the outer region and momentum is transported towards the wall, while the tail of the wake decelerates the outer layer. As the wake moves further into the domain, the outer layer gets accelerated, but the inner region responds more slowly due to the viscous effects. Hence, the wake increases the transport of mean momentum towards the wall. Those observations are consistent with the findings of [3, 18]. It is interesting that the streamwise pressure gradient at $t = 0.65\mathscr{T}$ changes sign close to the wall. This is a sign of the developing instability, which creates zones of positive and negative pressure gradients even before the vortices fully roll up. At the location of the figure, the vortices are still too weak to be seen in figure 3, but a detailed study of the phase-averaged pressure (not shown) clearly shows the pressure minima associated with the vortex cores.

Mean Flow Properties

The time-averaged mean flow properties are shown in Fig. 6a−e for APG flows with and without wakes. In the unperturbed case, a large unsteady separation bubble due to the adverse pressure gradient starts about $x/\theta_0 = 213$ and re-attaches at $x/\theta_0 = 721$. It can be seen in Fig. 6 that the unperturbed case results in a much longer region of separated flow than in

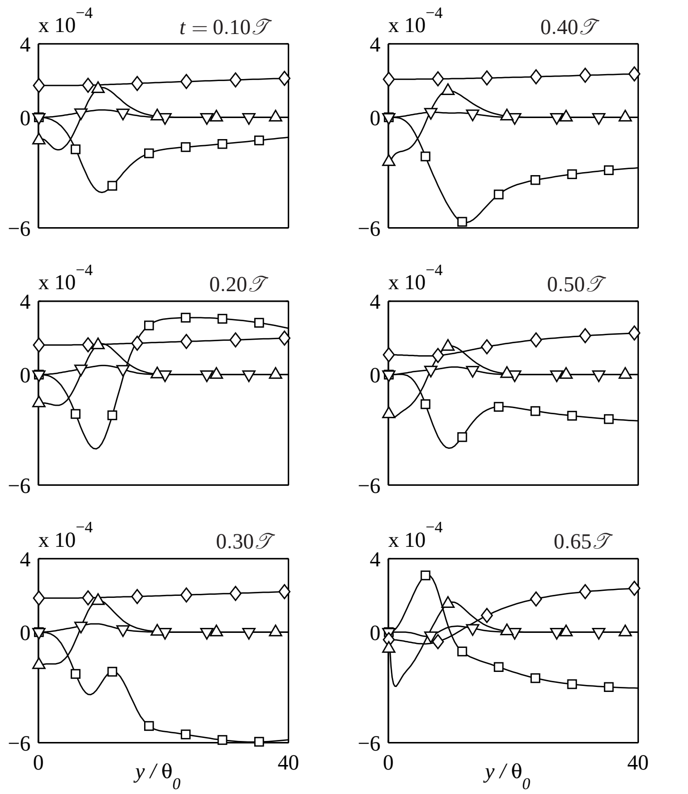

FIGURE 5. The phase-averaged streamwise momentum budget over one forcing period for case $\mathscr{W}4$ at $x/\theta_0 = 295$ (marked in Fig. 4). $\square$: Convective term $\partial_x\langle UU\rangle + \partial_y\langle UV\rangle$, ∇: Reynolds stress term $\partial_x\langle uu\rangle + \partial_y\langle uv\rangle$, $\diamond$: Pressure gradient term $\partial_x\langle P\rangle$, $\triangle$: Viscous term $1/Re(\partial_{xx} + \partial_{yy})\langle U\rangle$.

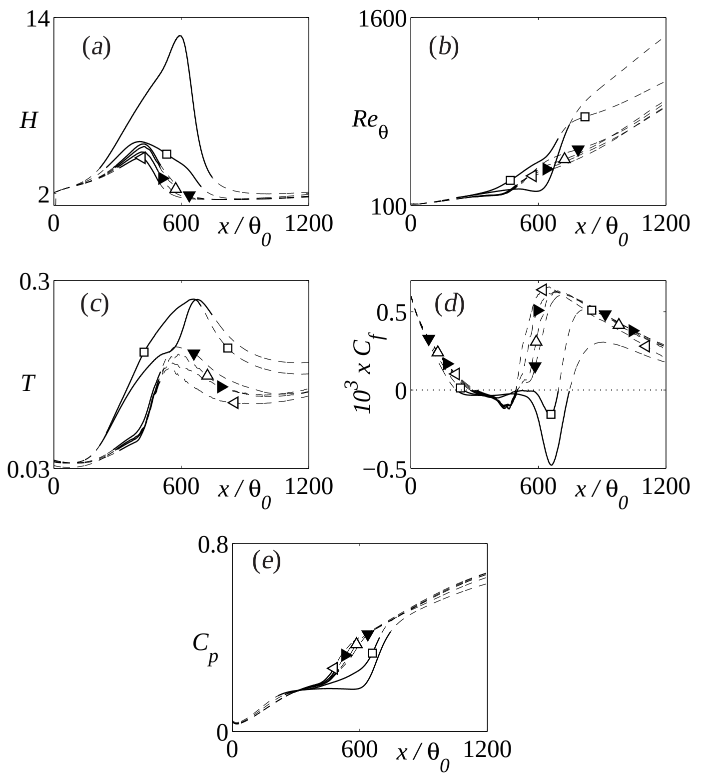

FIGURE 6. (a) Shape factor; (b) Reynolds number based on momentum thickness; (c) Maximum turbulent intensity; (d) Skin friction coefficient; (e) Wall pressure coefficient. no-symbol: $\mathscr{W}0$, $\square$: $\mathscr{W}1$, $\blacktriangledown$: $\mathscr{W}2$, $\triangle$: $\mathscr{W}3$, $\blacktriangleright$: $\mathscr{W}4$, $\triangleleft$: $\mathscr{W}5$, —— : separated flow, $C_f < 0$, and - - - - : attached flow, $C_f > 0$.

cases with inflow wakes. The effect of inflow perturbations can be seen on both ends of the bubble. Not only the reattachment point moves upstream, owing to transition to turbulence and hence increased wall normal mixing, but also the separation point moves downstream. This is due to a mean flow deformation by the wake transport of mean momentum towards the near-wall region. Figure 6a shows a comparison of the time-averaged shape factors, H, which increase rapidly at separation for the case without wakes. In the perturbed case, the wakes distort the boundary-layer development, resulting in a significant decrease in H. The streamwise variation of the maximum turbulent intensity, $T(x) = \max_y\left(\sqrt{\frac{1}{3}\left(\overline{u_i'u_i'}\right)}/U_\infty(x)\right)$, where $u_i' = \tilde{u}_i + u_i$ is shown in Fig. 6c. For the perturbed flow, the growth of the disturbances in the initial part of the separated region is slow, whereas they grow much faster in the downstream part of the separated region. This sudden growth of the streamwise fluctuations triggers a slowdown of bubble growth due to turbulent energy diffusion (see also Fig. 8e) and is responsible for the increase in C_f (Fig. 6d). The time-averaged skin friction coefficient distribution gives a quantitative measure of the bubble length, which has decreased significantly in the forced cases. Figure 6e shows the wall static pressure coefficient, C_p calculated based on a reference pressure and velocity at the free-stream of the outflow plane. The upstream C_p and C_f distributions are nearly identical for all cases, showing the dominant effect of the pressure gradient until instantaneous reverse flow occurs at the wall. Pressure increases steadily and reaches a constant level, which is then followed by a sharp recovery further downstream. The pressure plateau, identified as the dead-air region or the laminar part, indicates that the pressure in the initial part of the separated region is relatively constant. Results point out that a larger laminar separation region, as suggested by the plateau present in the C_p distribution, exists in the absence of any forcing and at very low forcing frequencies. In the perturbed cases with higher frequencies, however, the pressure plateau is still present, but significant only in a very small portion of the plate.

Figure 7 shows the normalized mean velocity profiles at different streamwise locations around the separation region. The time-averaged separation region is also indicated in the same plot with thick solid lines. The squares shown indicate the inflec-

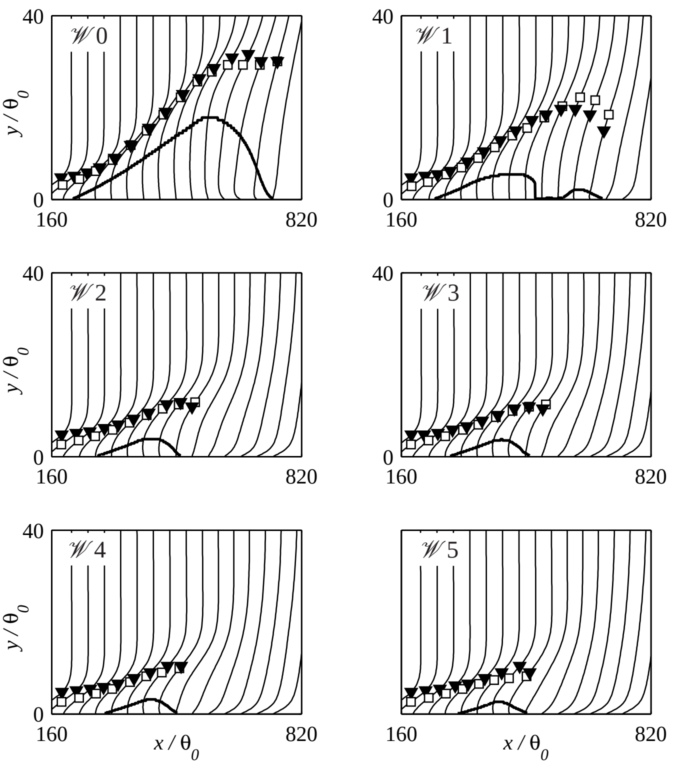

FIGURE 7. Mean streamwise velocity $\overline{U}$ profiles along the flat plate around the separated region for cases $\mathscr{W}0-\mathscr{W}5$ from left to right, top to bottom, respectively. □: Inflection points, and ▼ : Location of the maximum of the streamwise velocity intensity in the velocity profiles. The thick solid line in all figures is the zero contour of $\overline{U}$, and marks the locations of the separated region.

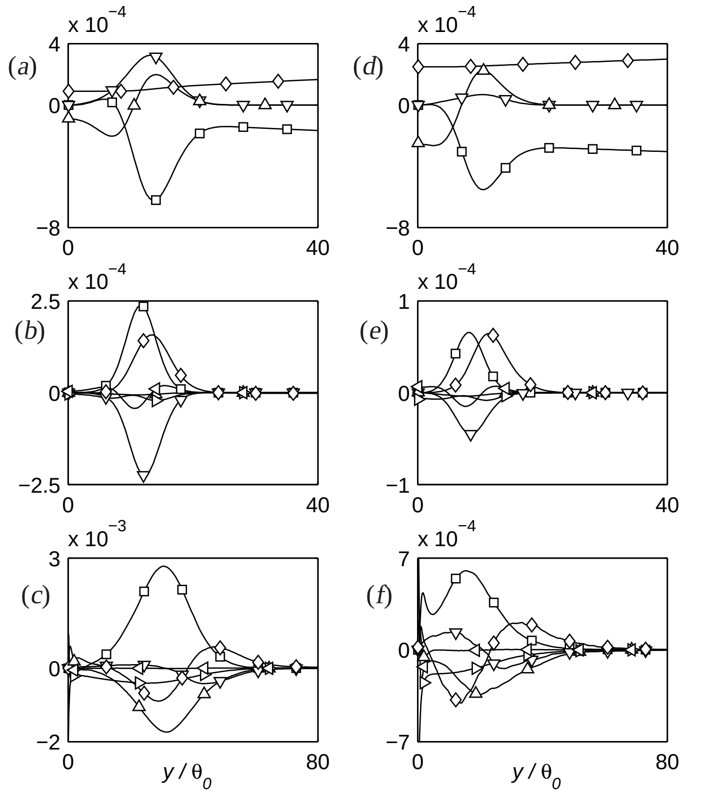

FIGURE 8. (a,d) Streamwise momentum budget at $x/\theta_0 = 295$. □: Convective term, ▽: Reynolds stress term, ◇: Pressure gradient term, △: Viscous term. Streamwise Reynolds stress balance at (b,e) $x/\theta_0 = 295$ and (c,f) $x/\theta_0 = 650$. □: Production: $-2\overline{u'\cdot\vec{u}'}\nabla\cdot\overline{U}$, ▽: Convection: $-\nabla\overline{u'u'}\cdot\vec{\overline{U}}$, ◇: Transport: $-\nabla\cdot\overline{u'u'\vec{u}'}$, △: Pressure transport: $-2\overline{u'\partial_x p'}$, ▷: Dissipation: $1/Re\nabla^2\overline{u'u'}$, ◁: Diffusion: $2/Re\overline{\nabla u'\cdot\nabla u'}$. (a,b,c) The unperturbed case ($\mathscr{W}0$). (d,e,f) The perturbed case ($\mathscr{W}2$).

tion points in the velocity profile. The profiles have an inflection point imposed by the APG, which is the precursor of the boundary layer separation. Flow fluctuations originate on the line of inflection points in the velocity profile. The line of inflection points is significant for the development of transition and reattachment. The location of maximum streamwise intensity at different streamwise locations is also shown in the same plot. It is seen that the maximum intensity matches approximately with the line of the inflection points up to the maximum height of the separation region. This can be explained by the fact that the large shear near the point of inflection enhances the energy transfer from the mean flow to the fluctuations. The shear-layer spreading in the reattachment region and the development of high velocity gradients near the wall in the turbulent region are clear. The separated region, shown by thick solid lines in the figures, becomes quite thin and short in the perturbed cases. The more significant difference is in the wall-normal extension of the separation bubble. For all cases, the maximum displacement of the bubble is located around the pressure recovery point (see Fig. 6e). Moreover the boundary layer transition takes place upstream of the maximum displacement, as shown by the occurrence of a local peak in the turbulence intensity plot (Fig. 6c).

The time-averaged streamwise momentum budget is illustrated in Fig. 8a and d at a streamwise location of $x/\theta_0 = 295$ for two cases $\mathscr{W}0$ and $\mathscr{W}2$, respectively. In the unforced case, $x/\theta_0 = 295$ is a streamwise position where the flow has separated, but transition to turbulence is not complete. In the forced case the flow has hardly separated at this position. Figure 8a depicts that inside the separated region all terms in the streamwise momentum equation are important. The Reynolds stress term starts to develop in the separated shear layer due to the inviscid instability, which is also depicted in Fig. 6c. At this position both the convective term and the Reynolds stress term dominate the streamwise momentum equation. At this position, $x/\theta_0 = 295$, the streamwise Reynolds stress budget shown in Fig. 8b indicates that the budget values are negligible with respect to ones further in the turbulent region (Fig. 8c). However, it can be observed that the production is amplified in the region of the high shear and that it is primarily balanced with convection and turbulent transport. In between this location and the position where the bubble reaches its maximum height ($x/\theta_0 \approx 650$, see Fig. 6c) a considerable increase in the budget terms is observed. The production term is really dominating the flow at this point. Some of this excess is transported towards the wall and the outer flow by turbulent transport, while another part is transferred by pressure transport to the other Reynolds stress terms. Turbulent diffusion is however the most important negative term at this position. At this position the Reynolds stress budget for the unforced flow has a typical shear layer appearance.

These observations for the unperturbed case $\mathscr{W}0$ can be extended also for the perturbed case ($\mathscr{W}2$). For case $\mathscr{W}2$ the streamwise location, $x/\theta_0 = 295$, is slightly downstream of the separation point. The streamwise momentum balance shown in Fig. 8d for this location illustrates that all the terms except the Reynolds stress term are important. At this location the shear layer is slightly shifted away from the wall. This separated shear layer introduces a small increase in the Reynolds stress term. The viscous term is significant in the near-wall region and balances the pressure term, whereas the convective term dominates the outer layer. The Reynolds stress budget shown in Fig. 8e illustrates qualitatively similar profiles as for case $\mathscr{W}0$ (Fig. 8b). This can easily be understood considering that in both cases the flow is separated and still has not reached transition at this location. However, significant difference is observed at $x/\theta_0 = 650$ (Fig. 8f). At this position the forced flow has already attached and developed in the turbulent region. The production has two peaks, one in the near-wall region and the other in the outer layer, which is the trace of the production that is generated in the shear layer that exists between the reverse-flow and the free-stream. Although not shown, it is important to note here that this outer peak decays as the flow moves further in the domain. The produced energy is transported toward to the wall by turbulent transport.

WAKE PROFILE EFFECT

The original flat plate experiment [8] has a favorable pressure gradient (FPG) region before the APG part. We are matching the inflow conditions correctly at the start of the APG region for the unperturbed case, but when we introduce the wake effect at the inflow, we are not including the wake acceleration due to the FPG or the so called stretching effect of the leading edge of the blade. In order to investigate the effect of the shape of incoming wakes, we have performed several experiments by modifying the wake profile, which is changed by varying its maximum velocity defect, U_{wd} and its symmetry, represented by the skewness parameter $\sigma = 1/n\sum_{i=1}^{n}(x_i - x_{wc})^3/(1/n\sum_{i=1}^{n}(x_i - x_{wc})^2)^{3/2}$, where x_{wc} is the wake center. The parameters of the new experiments along with the base case ($\mathscr{W}4$) for these experiments are given in table 2. All cases started from a restart file from case $\mathscr{W}4$ and run for 10 wake passing periods, and statistical results are obtained for another 10 wake passing periods. In the first two experiments, $\mathscr{R}1$ and $\mathscr{R}2$, the symmetry of the wake is conserved ($\sigma = 0$) but the mean wake deficit is varied, whereas in the last three experiments, $\mathscr{R}3$, $\mathscr{R}4$, and $\mathscr{R}5$, the symmetry is distorted while keeping the velocity defect constant. Based on the sign of the skewness parameter, the wake width is modified either in the front ($\sigma > 0$) or in the tail ($\sigma < 0$). The Strouhal number, St_{θ_b} of these experiments is 0.0265.

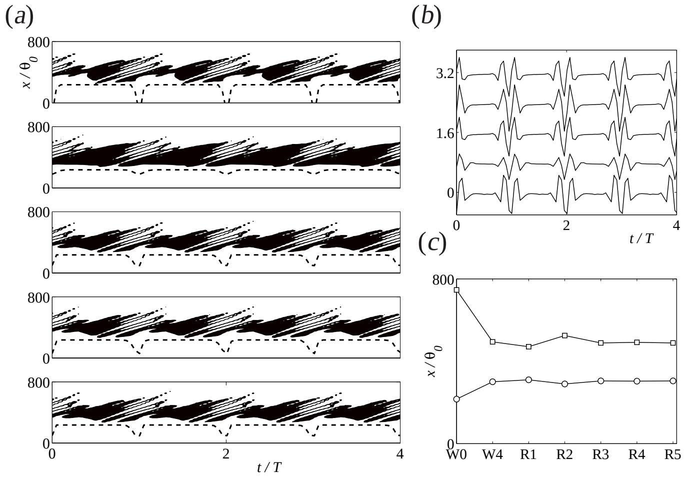

FIGURE 9. (a) The space-time development of the separated region and for cases $\mathscr{R}1 - \mathscr{R}5$ top to bottom, respectively. The dashed line indicates the mean wake deficit at the inflow, $x/\theta_0 = 0$. (b) The time history of the streamwise velocity just above the wall as a function of time at $x/\theta_0 = 426$, for cases $\mathscr{R}1 - \mathscr{R}5$ bottom to top, respectively. Data shifted vertically for visual clarity. (c) Separation (○) and reattachment (□) points.

Similar to the St number studies presented in the previous section, the Reynolds number based on the momentum thickness at separation Re_{θ_s} is about 168 and the non-dimensional pressure gradient Λ_s is in the range suggested by [14]. The space-time development of the separated region along with the streamwise

TABLE 2. Simulation parameters for the wake studies, $St_{\theta_b} = 0.0265$.

Case	σ	U_{wd}/U_{ref}	Re_{θ_e}	Re_{θ_s}	Λ_s	L_b/L_{b_0}
$\mathscr{W}4$	0	0.13	980	167	-0.118	0.3810
$\mathscr{R}1$	0	0.27	1101	168	-0.110	0.3163
$\mathscr{R}2$	0	0.04	1011	167	-0.123	0.4629
$\mathscr{R}3$	-1.8	0.13	989	169	-0.130	0.3624
$\mathscr{R}4$	-1.2	0.13	985	168	-0.120	0.3708
$\mathscr{R}5$	1.8	0.13	1001	169	-0.118	0.3519

velocity at the inflow (dashed lines) are illustrated in Fig. 9a for cases $\mathscr{R}1-\mathscr{R}5$. Wake profiles for each case can be identified easily from this figure. In case $\mathscr{R}1$ the wake has a strong maximum velocity defect but has a narrow width. On the contrary the wake in case $\mathscr{R}2$ has a small defect but wide width. The last three cases ($\mathscr{R}1-\mathscr{R}3$) have the same velocity defect but modified symmetry. Fig. 9a shows that separated region exist in all cases but its size varies in time and space based on the wake profile. The significant effect of the wake profile is observed for the first two cases. The strong wake in case $\mathscr{R}1$ effectively shortens the separated region whereas the weaker one in case $\mathscr{R}2$ does not modify it significantly except in the reattachment region. It is interesting that in all cases the shear layer instability is triggered. Similar to the *St* number studies, three roll-up vortices are generated in the separated region, and they convect downstream with half the local free-stream velocity. The traces of these vortices can be identified from Fig. 9b in which the development of the streamwise velocity at the first wall-point is demonstrated at a streamwise location, $x/\theta_0 = 426$ inside the time-averaged separated region.

The separation and reattachment locations for the time-averaged mean flow are shown in Fig. 9c for all cases along with base case $\mathscr{W}4$ and the unperturbed case $\mathscr{W}0$. The length of the separated region (see also table 2) is reduced significantly for the strong wake deficit case, $\mathscr{R}1$ in which the transition and hence the reattachment point moved upstream. On the other hand, it increased substantially for case $\mathscr{R}2$. In spite of the high local APG calculated in case $\mathscr{R}2$ (see table 2), the mean momentum towards the near-wall region is not strong enough to move the separation point downstream or to move the transition earlier. Hence, the length of the separated region increased significantly. It is interesting that the length of the separated region, along with the separation and reattachment locations are comparable with the one calculated for case $\mathscr{W}2$ (see table 1 and Fig. 2a) where the *St* number in that case is almost three times lower than the one considered in this experiment. The asymmetry of the wake does not have any dramatic effect on the size of the separated region (compared to the one for case $\mathscr{W}4$). However, a couple of interesting points are raised. As the wake tail gets stronger (case $\mathscr{R}3$), the local APG increases and hence this moves the separation point downstream. As a result, the length of the separated region shortens. At this point, it is important to note that the reattachment point is not affected dramatically with the change of the wake tail. On the contrary, it changes significantly as the wake front becomes steeper (case $\mathscr{R}5$). It is noted that the wake front does not have a significant role determining the separation location, whereas it becomes important in triggering the turbulence, hence controlling the reattachment location.

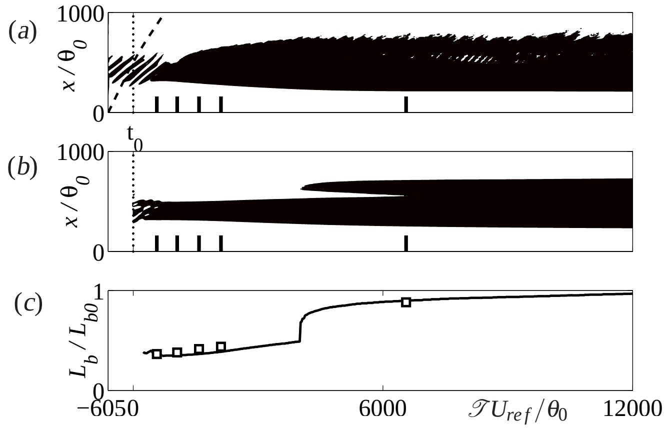

FIGURE 10. (a) The space-time development of the separated region. The dashed line traces the wake. (b) The space-time development of the time-averaged separated region. The thick solid lines mark the location of the numerical experiments. (c) The size of the separated region estimated from the regeneration experiment (——) and obtained from DNSes (□:$\mathscr{W}0-\mathscr{W}5$).

REGENERATION of the SEPARATED REGION

It is important to predict the size of the separated region for various forcing frequencies. If the passing frequency is low, such as in case $\mathscr{W}1$, the separation has more time to re-establish itself. Therefore, there will be a larger separated region between the inflow perturbation that will result in a larger profile loss. One way to predict the size of the separated region is to perform experiments for a wide range of frequencies. Even though this is feasible with real experiments, it is computationally expensive.

In order to find a cheaper way to predict the size of the separated region we performed one regeneration experiment. This numerical experiment is initiated with a restart file from a simulation with incoming wakes ($\mathscr{W}5$), and evolved further in time without imposing the wakes. In the absence of the wakes, the flow returns to the unperturbed condition as the simulation progresses. The idea is that by measuring the time that the unperturbed separated bubble needs to completely regenerate itself, it is possible to predict the influence of lower forcing frequencies, which would be expensive to simulate numerically.

The regeneration of the separation bubble is portrayed in Fig. 10a as the space-time development of the spanwise-averaged streamwise velocity, $U(x,t)$, just above the wall. The time required for the separation bubble to regenerate itself is around $5000\theta_0/U_{ref}$, where the length of the bubble at this time is $537\theta_0$, which is comparable with the length of the time-averaged bubble for the unperturbed case $\mathscr{W}0$, $L_b = 508\theta_0$. The discrepancy comes from the fact that the latter is averaged both in time and in span whereas the first one is obtained at one time instant and averaged only in the span.

This regeneration experiment is used to approximate the size of the separated region of the forced cases. The estimated bubble sizes are formed by averaging in time as well as in the spanwise direction. The time-averaging, $\overline{u}(x,\mathscr{T}) = \mathscr{T}^{-1}\int_{t_0}^{t_0+\mathscr{T}} U(x,t)dt$, is performed over the spanwise-averaged data, $U(x,t)$ of the regeneration experiment, depicted in Fig. 10a, and starts at time t_0 when the last wake is located approximately above the reattachment point of the time-averaged bubble for case $\mathscr{W}5$. The trace of the last wake and the initial time t_0 for the time-averaging are also shown in Fig. 10a. The development of the separated region of the time-averaged velocity $\overline{u}(x,\mathscr{T})$ is presented in Fig. 10b. The traces of the three vortices triggered in the separated region due to the last wake can be clearly seen for $\mathscr{T}U_{ref}/\theta_0 < 565$ as three disconnected separated regions in the time-averaged data. As the time integration range increases, the first part of the separated region forms. Note that, its size stays small in the first part of the regeneration, whereas it increases significantly afterwards. The second bubble that appear later can be related to the large negative peak in C_f which indicates the big recirculation region when the bubble transitions and reattaches.

Figure 10c shows the non-dimensional bubble length, along with the calculated ones from our DNSes. It is interesting that the approximated bubble size and the calculated ones are quite close to each other, underscoring the usefulness of the regeneration experiment.

LINEAR STABILITY ANALYSIS

Assuming a parallel base flow, the response of the boundary layer to small-amplitude perturbations, given in the form of $v = \hat{v}(y)e^{i(\alpha x-\omega t)}$, where α is the real wavenumber and $\omega = \omega_r + i\omega_i$ is the complex frequency of the travelling wave, can be predicted by solving the Orr-Sommerfeld equation. The disturbances are damped for $\omega_i < 0$, and amplified for $\omega_i > 0$. The parallel base flow approximation implies that the stability at a particular location is determined by local conditions. Therefore, disturbances with wavelengths much longer than the characteristic length scale of the problem (e.g., the bubble length) should be discarded.

Using velocity profiles extracted from time-averaged DNS data of the unperturbed case $\mathscr{W}0$, and perturbed cases $\mathscr{W}2$, and $\mathscr{W}4$ a linear stability analysis is performed at each streamwise location to determine the amplification rate of locally unstable disturbances. The stability diagram of the unperturbed case, illustrated in Fig. 11a shows the range of amplified waves as a function of streamwise location, $(x-x_S)/L_{b_0}$, where x_S is the separation point for unperturbed case. There are no unstable modes in the first part of the boundary layer, but they are there as soon as the profiles have inflection points. The maximum growth rate of the unstable modes increases linearly with x in the first part of the separated region, and has a maximum downstream of the location of maximum reverse flow, and decreases further downstream. In the framework of the spatial instability

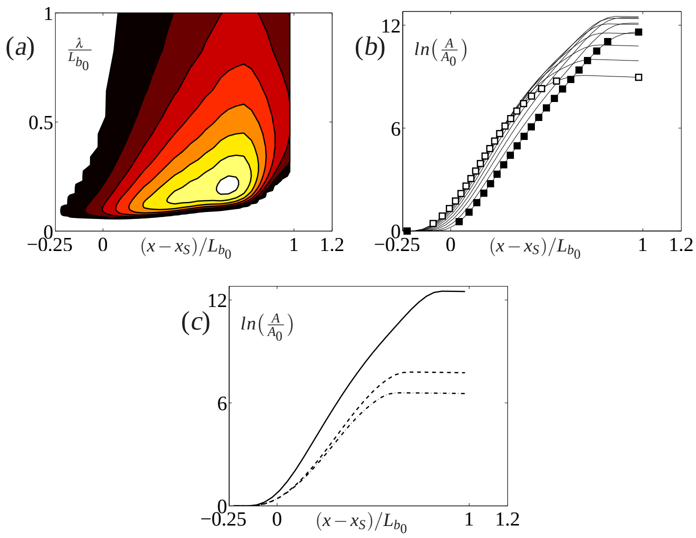

FIGURE 11. (a) Growth rate of the unstable modes $\alpha c_i = \mathrm{Im}(\omega)$ as a function of $(x-x_S)/L_{b_0}$ (b) Amplification of the unstable modes within the range of $\lambda/L_{b_0} = 0.10$ (□) and 0.27 (■). (c) Amplification of the unstable modes for the most amplified wavelengths: ——— : $\mathscr{W}0$; – – – – : $\mathscr{W}2$; – · – : $\mathscr{W}4$.

theory [19], the total amplification of a disturbance over a distance $x - x_0$ can be expressed as $A/A_0 = exp\left(\int_{x_0}^{x} \omega_i(x)/c_g dx\right)$, where $c_g = \partial\omega_r/\partial\alpha$. The streamwise variation of the natural logarithm of A/A_0 is plotted in Fig. 11b for the non-dimensional wavelengths, λ/L_b within the range of 0.10 and 0.27. Those wavelengths are strongly amplified in the region of the separated shear layer. The maximum amplification is obtained at $\lambda/L_b = 0.1754$, 0.1484, and 0.1411 for cases $\mathscr{W}0$, $\mathscr{W}2$, and $\mathscr{W}4$, respectively and the amplification curve at these maximums are illustrated Fig. 11c. The longer wavelengths are left out off the discussion since they are on the order of the bubble size, hence they would not satisfy the parallel base flow approximation.

Figure 12a shows the range of unstable wavelengths that are most amplified for all cases. It is observed from Fig. 12b that these wavelengths are in the range of wavelengths of the three vortices obtained from our DNSes. This further supports our observation that the vortices generated in the separated shear layer are due to the triggering of the inviscid instability.

The mode with highest amplification is portrayed in Fig. 13 for profiles located in the first part of the separated region. The height of the rolling structures increases with x, which agrees well with the observations from our DNS. The perturbations peak at the inflection point of the profiles. The rolling structures are centered around the inflection point and they are distorted close to the wall. Their predicted convection velocity is approximately half the free-stream velocity, which is also in reasonable agreement with our observations, the rollers propagate with half of the local free-stream velocity.

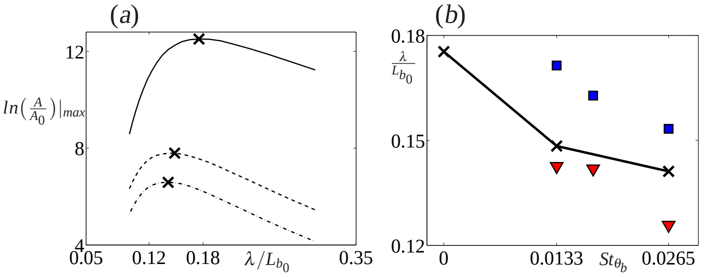

FIGURE 12. (a) Maximum of the total amplification of the unstable modes: —— :$\mathscr{W}0$; – – – – : $\mathscr{W}2$; – · – : $\mathscr{W}4$. (b) Most amplified wave lengths predicted from LSA (—×—) and from DNSes (□ and ▽).

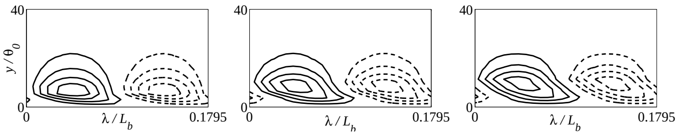

FIGURE 13. *u*-*v* perturbation streamlines at $(x-x_s)/L_{b_0} = 0.034$, 0.2, and 0.3. The solid lines correspond to clockwise-rotating rollers.

CONCLUSIONS

We analyze the response of the separated boundary layer to the passing wakes in terms of two parameters, frequency and shape. The frequency of the forcing strongly affects the time dependent location of the separation and re-attachment, but, no significant variations are observed for the mean boundary layer properties, unless the separation bubble is allowed to fully re-form. The details of the wake shape and velocity deficit characteristics do not change the flow development significantly. For all forcing frequencies and wake shapes studied here there are always three roll-up vortices generated in the unsteady shear layer. They travel downstream with a convective velocity of approximately half the free-stream velocity. The phase-averaged characteristics of the flow reveals that those vortices are generated in the separated shear layer due to triggering of an inviscid Kelvin-Helmholtz instability. The separation moves downstream by the effect of momentum carried by the wakes, while the reattachment moves upstream by the entrainment of those structures. It is noted that the separation among the roll-up vortices does not depend on the passing frequency of the wakes. A comparison of stability calculations and DNS results suggest that the wavelength of the most amplified disturbances in the separated shear layer and their propagation speed can be adequately estimated by linear stability theory.

A single recovery experiment is performed to predict the size of the separated region of the forced cases. After switching off the wake forcing and progressing further in time, the separated region regenerates itself to the unforced situation. The temporal development of the separated region is used to estimate the bubble lengths associated with the different wake passing frequencies, which agree well with those calculated from the DNSes.

An obvious future extension would be to extend this analysis to different pressure distributions, but it is probably preferable to check first whether the same regeneration experiment can be used to predict other properties of the separated region, such as, Re_{θ_s} and Λ_s.

This will be the next step in our program. In the mean time, the statistics from the present work will be gathered and made publicly available, particularly the Reynolds stress and energy budgets. This might assist in the formulation of better turbulence models, which are the essential parts of practical codes for the aeronautical and turbomachinery industries.

ACKNOWLEDGMENT

This work was supported in part by the CICYT grant TRA2009-11498, and by the SyeC CONSOLIDER. The computations were made possible by generous grants of computer time from the Barcelona Supercomputing Centre.

REFERENCES

[1] Wu, X., Jacobs, R., Hunt, J., and Durbin, P., 1999. “Simulation of boundary layer transition induced by periodically passing wakes”. *Journal of Fluid Mechanics*, ***398***, pp. 109–153.

[2] Wissink, J., and Rodi, W., 2006. “Direct numerical simulation of flow and heat transfer in a turbine cascade with incoming wakes”. *Journal of Fluid Mechanics*, ***569***, pp. 209–247.

[3] Hodson, H., and Howell, R., 2005. “Bladerow interactions, transition, and high-lift aerofoils in low-pressure turbines”. *Annual Review of Fluid Mechanics*, ***37***, pp. 71–98.

[4] Pauley, L., Moin, P., and Reynolds, W., 1990. “The structure of two-dimensional separation”. *Journal of Fluid Mechanics*, ***220***, pp. 397–411.

[5] Watmuff, J., 1999. “Evolution of a wave packet into vortex loops in a laminar separation bubble”. *Journal of Fluid Mechanics*, ***397***, pp. 119–169.

[6] Dovgal, A., Kozlov, V., and Michalke, A., 1994. “Laminar boundary layer separation: instability and associated phenomena”. *Progress in Aerospace Sciences*, ***30***, pp. 61–94.

[7] Alam, M., and Sandham, N., 2000. “Direct numerical simulation of short laminar separation bubbles with turbulent reattachment”. *Journal of Fluid Mechanics*, ***410***, pp. 1–28.

[8] Zhang, X., and Hodson, H., 2005. “Combined effects of surface trips and unsteady wakes on the boundary layer development of an ultra-high-lift LP turbine blade”. *Journal of Turbomachinery*, ***127***, pp. 479–488.

[9] Simens, M., Jiménez, J., Hoyas, S., and Mizuno, Y., 2009. “A high-resolution code for turbulent boundary layers”. *Journal of Computational Physics*, ***228***, pp. 4218–4231.

[10] Simens, M., 2009. "The study and control of wall bounded flows". PhD thesis, Universidad Politécnica de Madrid, Spain.
[11] Schlichting, H., 1979. *Boundary-Layer theory*. Mc Graw-Hill.
[12] Gaster, M., 1967. "The structure and behaviour of separation bubbles". In ARC London Reports and Memoranda.
[13] Thwaites, B., 1949. "Approximate calculation of the laminar boundary layer". *Aero. Q.*, ***1***, pp. 61–85.
[14] Curle, N., and Skan, S. W., 1957. "Approximate methods for predicting separation properties of laminar boundary layers". *Aero. Q.*, ***8***, pp. 257–268.
[15] Monkewitz, P., and Huerre, P., 1982. "Influence of the velocity ratio on the spatial instability of mixing layers". *Physics of Fluids*, ***25***, pp. 1137–1143.
[16] Michalke, A., 1964. "On the inviscid instability of the hyperbolic-tangent velocity profile". *Journal of Fluid Mechanics*, ***19***, pp. 543–556.
[17] Stieger, R., Hollis, D., and Hodson, H., 2003. "Unsteady surface pressures due to wake induced transition in a laminar separation bubble on a LP turbine cascade". *Journal of Turbomachinery*, ***126***, pp. 544–550.
[18] Stieger, R., and Hodson, H., 2003. "The transition mechanism of highly-loaded LP turbine blades". *ASME Turbo Expo Paper GT-2003-38304*.
[19] Arnal, D., 1993. "Boundary layer transition: Prediction based on linear theory". In AGARD Report No. 793, pp. 2.1–2.63.